



**EUROfusion**

WPTR-CPR(18) 20908

M. Cavedon et al.

**On the ion and electron temperature  
recovery after the ELM-crash at ASDEX  
Upgrade**

Preprint of Paper to be submitted for publication in Proceeding of  
23rd International Conference on Plasma Surface Interactions in  
Controlled Fusion Devices (PSI-23)



This work has been carried out within the framework of the EUROfusion Consortium and has received funding from the Euratom research and training programme 2014-2018 under grant agreement No 633053. The views and opinions expressed herein do not necessarily reflect those of the European Commission.

This document is intended for publication in the open literature. It is made available on the clear understanding that it may not be further circulated and extracts or references may not be published prior to publication of the original when applicable, or without the consent of the Publications Officer, EUROfusion Programme Management Unit, Culham Science Centre, Abingdon, Oxon, OX14 3DB, UK or e-mail [Publications.Officer@euro-fusion.org](mailto:Publications.Officer@euro-fusion.org)

Enquiries about Copyright and reproduction should be addressed to the Publications Officer, EUROfusion Programme Management Unit, Culham Science Centre, Abingdon, Oxon, OX14 3DB, UK or e-mail [Publications.Officer@euro-fusion.org](mailto:Publications.Officer@euro-fusion.org)

The contents of this preprint and all other EUROfusion Preprints, Reports and Conference Papers are available to view online free at <http://www.euro-fusionscipub.org>. This site has full search facilities and e-mail alert options. In the JET specific papers the diagrams contained within the PDFs on this site are hyperlinked

# On the ion and electron temperature recovery after the ELM-crash at ASDEX Upgrade

M. Cavedon<sup>a</sup>, R. Dux<sup>a</sup>, T. Pütterich<sup>a</sup>, E. Viezzer<sup>b</sup>, E. Wolfrum<sup>a</sup>, M. Dunne<sup>a</sup>, E. Fable<sup>a</sup>, R. Fischer<sup>a</sup>, G. F. Harrer<sup>c</sup>, F. M. Laggner<sup>d</sup>, A. F. Mink<sup>a,e</sup>, U. Plank<sup>a</sup>, U. Stroth<sup>a,e</sup>, M. Willensdorfer<sup>a</sup>, ASDEX Upgrade Team<sup>f</sup>

<sup>a</sup>Max Planck Institute for Plasma Physics, Boltzmannstr. 2, 85748 Garching, Germany

<sup>b</sup>Dept. of Atomic, Molecular and Nuclear Physics, University of Seville, 41012 Seville, Spain

<sup>c</sup>Institute of Applied Physics, TU Wien, Fusion@ÖAW, 1040 Vienna, Austria

<sup>d</sup>Princeton University, Princeton, NJ 08544, United States of America

<sup>e</sup>Physik-Department E28, Technische Universität München, 85748 Garching, Germany

<sup>f</sup>see the author list “A. Kallenbach et al, Nucl. Fusion 57, 102015 (2017)”

---

## Abstract

The access to fast measurements, i.e.  $\Delta t \approx 100 \mu\text{s}$ , of the ions and the electrons during an entire edge localized cycle (ELM) revealed asymmetries in the recovery of the maximum edge gradients. Different magnetic fluctuations are found to correlate with the saturation of the edge ion temperature ( $T_i$ ), electrons temperature ( $T_e$ ) and density ( $n_e$ ) gradients. In particular, while  $\nabla T_i$  and  $\nabla n_e$  clamp roughly 3.0 ms after the ELM-crash together with the onset of mid-frequency ( $f \lesssim 50 \text{ kHz}$ ) magnetic fluctuations,  $\nabla T_e$  recovers to the pre-ELM conditions only after 7.0 ms and saturates with the appearance of high frequency fluctuations ( $f \approx 200 \text{ kHz}$ ). Two hypotheses for the delayed recovery of  $\nabla T_e$  are discussed: the onset and the suppression of electron temperature gradient modes (ETGs) qualitatively follow the requirements of an increased electron heat transport. However, gyro-kinetic simulations are necessary to quantify the impact of ETGs. On the other hand, the impact of the neutral ionization during the density build-up as an electron energy loss channel is measured to be small compared to the total electron energy. The dominant terms in the electron energy balance are instead the radiative power and the ion-electron heat exchange.

*Keywords:*

---

## 1. Introduction

The fusion performance of any future reactor is closely related to the pressure at the top of the pedestal [1]. In the high confinement mode (H-mode), however, the edge localized mode (ELM) limits the growth of the pedestal by periodic relaxations of the steep gradient at the edge of the plasma. Moreover, the energy and particle fluxes flushed to the plasma facing components during

ELMs pose one of the most serious technical challenges for future devices. For these reasons, ELMs have been an active subject of research since the discovery of the H-mode [2].

While the peeling-ballooning theory is successfully employed to describe the stability limit of the pedestal [3], the prediction of the evolution of the pedestal shape (height and width) in between ELMs, the so-called inter-ELM phase, needs additional constraints. Gyro-kinetic simulations indicate that the pre-ELM pedestal conditions are unstable with respect to several micro-instabilities of which micro-tearing modes (MTMs) and ki-

---

*Email address:* marco.cavedon@ipp.mpg.de (M. Cavedon)

netic ballooning modes (KBM) are the dominant instabilities [4, 5, 6]. The onset of the latter is employed to limit the maximum achievable pressure gradient in the EPED model [7]. However, in the inter-ELM profile recovery other instabilities come into play, such as electron temperature gradient (ETG) modes and trapped electron modes (TEM) [8].

Several tokamaks reported on the rise of density and magnetic fluctuations during the pedestal recovery [9, 10, 11]. Their high frequency component correlates with the clamping of the maximum electron pressure gradient suggesting a KBM nature [9]. However, their existence at the high field side indicates a non-ballooning behavior [10]. At the same time, a good agreement is found by comparing experimentally determined toroidal mode numbers and non-linear MHD simulations during the ELM [12].

In this work, the evolution of the ion temperature and impurity flows during the ELM cycle are analyzed. These parameters are often missing in ELM studies due to the demanding diagnostic requirements. By means of ultra-fast charge exchange (CX) measurements, the study in [13] could be extended to different impurity species. Comparison to magnetic probe measurements shows a correlation between the profile behaviour of ions and electrons and the onset of magnetic fluctuations (see section 2). Furthermore, two hypotheses are discussed for the delayed recovery of the electron temperature gradient  $\nabla T_e$  and compared to the electron density  $\nabla n_e$  and ion temperature gradient  $\nabla T_i$  [13, 14]. To this end, interpretative transport simulations are designed to quantify the energy sources and sinks during the ELM-recovery (section 3). Finally, the conclusions and the outlook are given in section 4.

## 2. Correlating the recovery of the ion and electron profiles to magnetic fluctuations

ELM-resolved electron temperature and density profiles are routinely measured in several machines [15, 16, 17, 14], while information on the

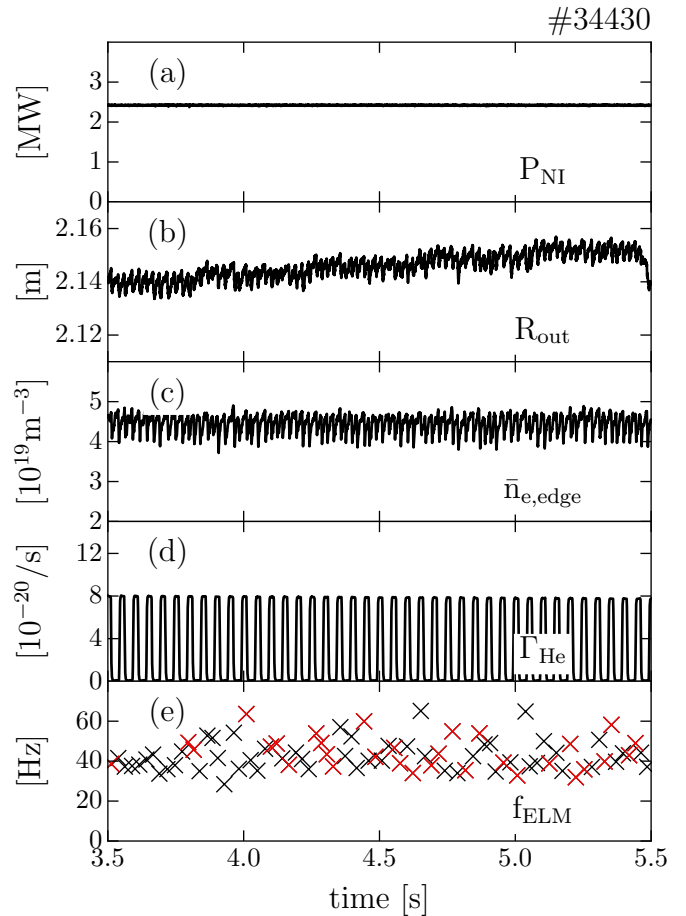


Figure 1: Timetraces of a reference discharge: (a) neutral beam input power, (b) outer midplane plasma position, (c) line average edge density, (d) helium seeding rate, (e) ELM frequency (the red crosses indicate the ELM selected for the synchronization).

ion and flow profiles are often not accessible. Recent developments of fast CX systems allow sub-ms measurements of the edge ion temperature, impurity flows and, via the radial force balance equations, of the  $\mathbf{E} \times \mathbf{B}$  velocity,  $v_{\mathbf{E} \times \mathbf{B}}$  [18, 19]. These are of particular interest given the connection between  $v_{\mathbf{E} \times \mathbf{B}}$  and the pedestal formation [20] and of the  $T_i/T_e$  ratio on the pedestal stability [21]. ELM-resolved ion and electron temperature measurements revealed asymmetries between the  $e$ - and  $i$ -channels during the ELM-crash and the recovery [13]. At the ELM-crash, the ion temperature in the vicinity of the separatrix increases such that  $T_i/T_e \approx 5$  [22] indicating that the parallel ion heat transport is not negligible and can be comparable to that of the electrons in

the SOL [23]. Furthermore, the recovery of  $\nabla T_i$  after the ELM-crash appears to be faster than the one of  $\nabla T_e$  and on the same time scale as  $\nabla n_e$  [13]. Finally, the radial electric field  $E_r = v_{E \times B} \cdot B$  drops to typical L-mode like values at the ELM-crash and it recovers to the pre-ELM conditions on the same time scales as  $\nabla n_e$  and  $\nabla T_i$ .

Comparing the ion and electron profiles to the magnetic data reveals a correlation between the evolution of the ion and electron gradients and the onset of magnetic fluctuations. Several discharges were designed to obtain detailed profiles at the edge of the plasma at the lowest ELM frequency possible to better separate the recovery phases. This has been achieved with high triangularity discharges, at a toroidal field of  $-2.5$  T, plasma current of  $0.8$  MA and with an input power just above the L-H power threshold but sufficient for type-I ELMs [24]. Figure 1 shows the time traces of the total neutral input power  $P_{NI}$  (a), the outer midplane plasma position  $R_{out}$  (b), the line average density  $n_{e,edge}$  (c), the applied helium gas puff  $\Gamma_{He}$  (d), and the ELM frequency  $f_{ELM}$  (e) for the reference discharge. The helium puffs are necessary to increase the signal to noise ratio for the fast CX measurements, e.g. at a time resolution of  $100 \mu s$ . A plasma phase has been selected for the analysis in which the input power and density are constant (figures 1a and 1c). During this time window, the plasma has been swept radially to increase the radial coverage of the edge diagnostics (figure 1b). The resulting ELM frequency is about  $40$  Hz (figure 1d) which offers long inter-ELM phases, ideal for the analysis of the profile recovery. In figure 1d the red crosses indicate the 31 ELMs used for the following analysis. The selection is based on the maximum cross-correlation of the divertor shunt current  $I_{div}$  of a reference ELM with the other ELMs in the time window. An arbitrary threshold on the cross-correlation of  $0.98$  has been used to select ELMs whose induced divertor current are similar. The synchronized  $I_{div}$  is shown in figure 2g. Note that the synchronization procedure introduces scatter which depends on the specific temporal resolution of a signal. In this work, the electron and ion diagnostics are sampled at a time resolution of  $100 \mu s$

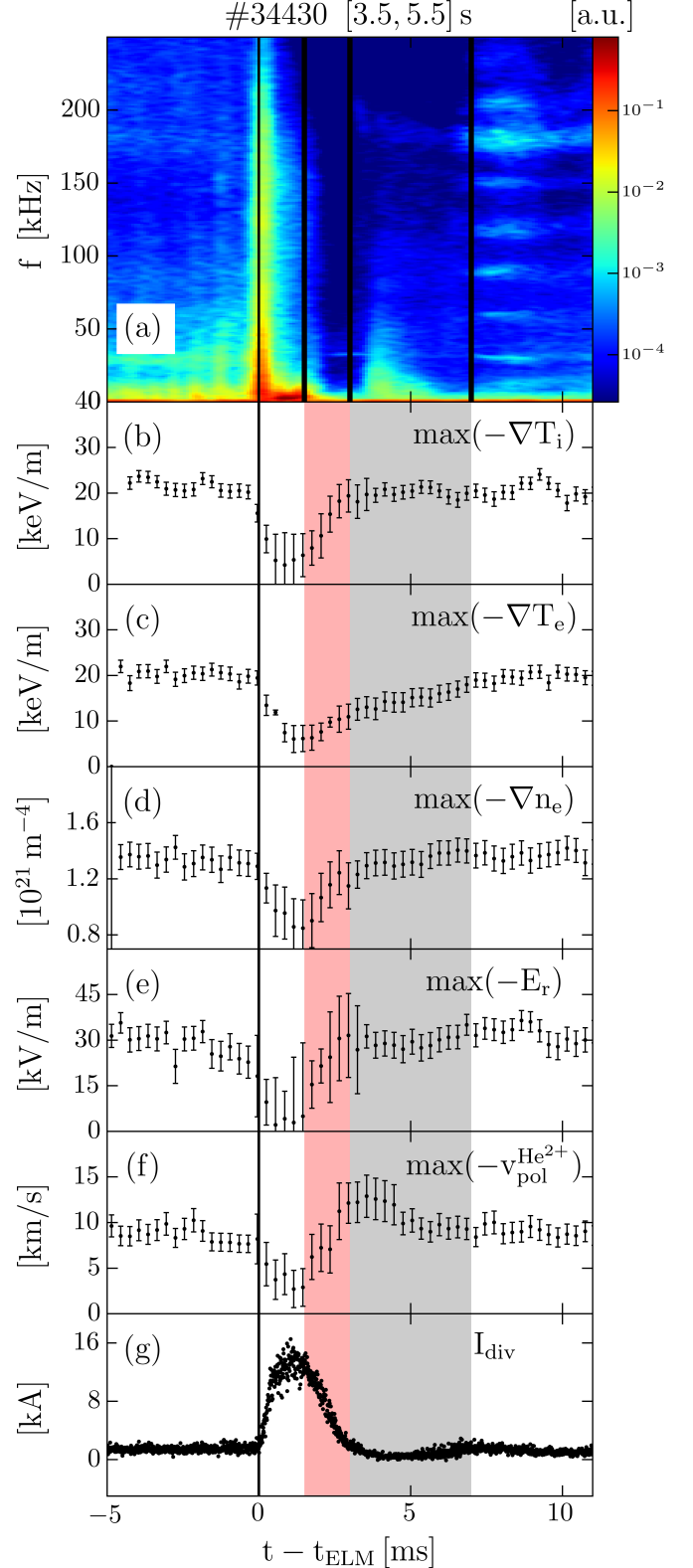


Figure 2: Comparison of the magnetic fluctuations with the profile gradient recovery (all the signals are ELM-synchronized): (a) Spectrogram of an outer midplane BAL-coil, (b)  $\max(-\nabla T_i)$ , (c)  $\max(-\nabla T_e)$ , (d)  $\max(-\nabla n_e)$ , (e)  $\max(-E_r)$ , (f)  $\max(-v_{pol}^{He^{2+}})$ , and (g)  $I_{div}$ .

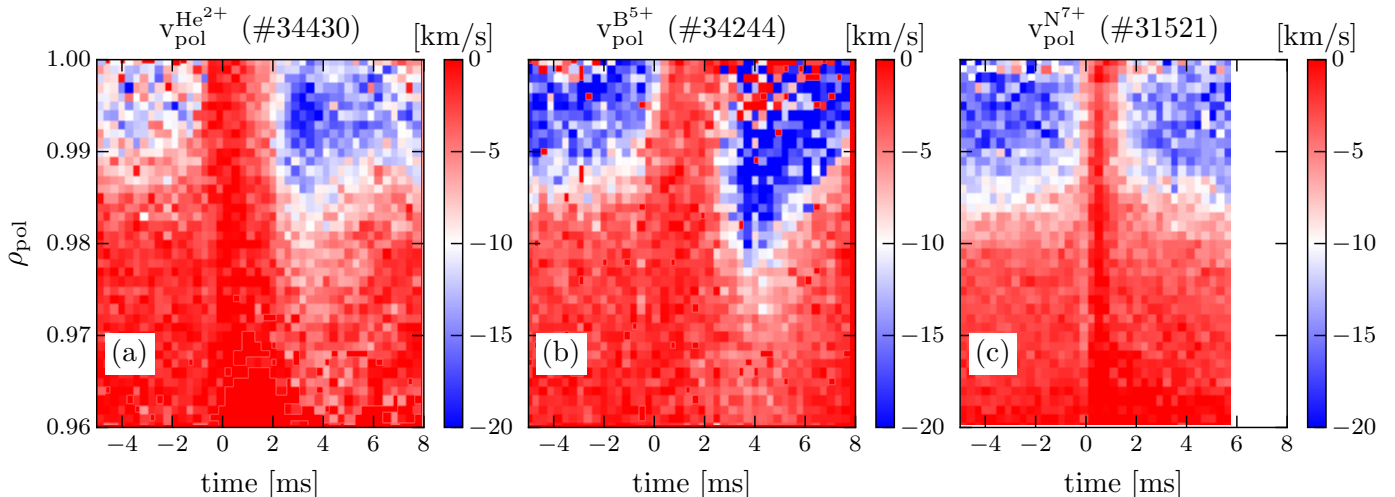


Figure 3: ELM-synchronized poloidal velocity profiles of  $\text{He}^{2+}$  (a),  $\text{B}^{5+}$  (b) and  $\text{N}^{7+}$  (c). Note that the data are taken in different discharges with different seeding conditions and ELM frequencies.

which results in an uncertainty of  $300 \mu\text{s}$  due to possible mis-synchronization of a single frame. To avoid confusion, all the measurements presented later are re-binned to this time resolution.

Following the analysis procedure described in [13], the ELM-synchronized maximum gradients of  $T_i$ ,  $T_e$  and  $n_e$  are shown in figures 2b, 2c and 2d, respectively. Moreover, the minimum of the radial electric field, determined from the radial force balance for  $\text{He}^{2+}$ , is presented in figure 2e and the maximum of the poloidal velocity of the fully ionized helium  $v_{\text{pol}}^{\text{He}^{2+}}$  is shown in figure 2f. The divertor shunt current  $I_{\text{div}}$  is used as a reference signal for the synchronization (fig. 2g). The profile gradients are compared to the ELM-synchronized spectrogram from a toroidal ballooning pick-up (BAL-) coil placed at the outer midplane (figure 2a). The spectrogram shows the typical pattern as described in [10, 12]: at the ELM crash a strong broadband magnetic activity is observed ( $t \in [0, 1.5]$  ms) followed by a quiet phase ( $t \in [1.5, 3.0]$  ms). Between roughly 3.0 and 7.0 ms magnetic activity with frequency up to 50 kHz re-appears. This is then replaced, after 7 ms, by fluctuations with dominant frequency around 180 kHz and several other distinct frequencies. The high frequency magnetic fluctuations can get weaker before the ELM ( $t < 0$  ms) as already observed in [12]. Note that the quiet phase between 1.5 and 3.0 ms coincides with the

recovery of  $\nabla T_i$ ,  $\nabla n_e$  and  $E_r$  (see red shaded area) to the pre-ELM values while the reestablishment of  $\nabla T_e$  lasts until the onset of the high frequency fluctuations at  $t = 7$  ms (see gray shaded area). According to the relation presented in [10], the pre-ELM value of the edge radial electric field ( $\approx -30$  kV/m, fig. 2e) is consistent with the dominant magnetic fluctuation frequency of 180 kHz suggesting that the observed modes have the same nature.

The minimum of the  $\text{He}^{2+}$  poloidal velocity (fig. 2e) is first decreased by the ELM, then recovers and becomes even larger than the pre-ELM value for a short time. This has been observed before in [13]. Note that the poloidal velocity of a plasma species  $\alpha$  is a critical contribution in the radial force balance since it is multiplied by the toroidal field  $B_{\text{tor}}$ :

$$E_r = \frac{\nabla_r(n_\alpha T_\alpha)}{eZ_\alpha n_\alpha} + v_{\text{tor},\alpha} B_{\text{pol}} - v_{\text{pol},\alpha} B_{\text{tor}} \quad (1)$$

In the edge of ASDEX Upgrade (AUG) the toroidal velocity  $v_{\text{tor},\alpha}$  is small [25], therefore  $v_{\text{pol},\alpha}$  is the dominant contribution for medium- to high-Z species because the diamagnetic term, i.e. the first term in the eq. (1), is divided by the charge  $Z_\alpha$ . In the case of  $\text{He}^{2+}$ , both the diamagnetic and the poloidal velocity contribution are important for the determination of  $E_r$ . Therefore, the spin-up in  $v_{\text{pol},\alpha}$  is not necessarily reflected in

the reconstruction of  $E_r$ . In figure 3, the ELM-synchronized poloidal velocity of  $\text{He}^{2+}$  (a),  $\text{B}^{5+}$  (b) and  $\text{N}^{7+}$  (c) are compared. The poloidal velocity of  $\text{B}^{5+}$  and of  $\text{N}^{7+}$  do not exhibit the same spin-up as  $v_{\text{pol}}^{\text{He}^{2+}}$ , consistent with the  $E_r$  measurements because for  $Z_\alpha = 5, 7$ ,  $E_r$  is approximately  $-v_{\text{pol},\alpha} B_{\text{tor}}$ . However, the measurements of the different poloidal velocities are obtained in different conditions and time resolutions. Namely, the use of nitrogen seeding increases  $f_{\text{ELM}}$  [26, 27] and hence a match of the ELM-cycle duration with the reference case was not possible. Furthermore, fast CX measurements, i.e.  $\Delta t \approx 100 \mu\text{s}$ , were only possible in discharges with He and N seeding while an exposure time of 2.3 ms has been employed when measuring boron. This is because external seeding of  $\text{B}_2\text{H}_6$  at the time and the intrinsic B leads to a limited signal.

The asymmetry in the time scales of the ELM-recovery of the ion and electron maximum temperature gradients has been first observed in [13] and confirmed in [28] by means of main ion CX measurements. Note that this also implies a good thermalization of the impurity. On the other hand, the different behavior of electrons and ions is puzzling. The delay in the recovery of  $\nabla T_e$  must be due to either an enhanced electron heat transport, an additional energy loss or a combination of both. In particular, the possible effect of electron temperature gradient modes (ETGs) as electron heat transport mechanism or the effect of neutrals as energy loss are discussed in the next section.

### 3. On the delayed recovery of the electron temperature gradient

In this section, two possible mechanisms for the delayed recovery of  $\nabla T_e$  are examined: electron temperature gradient modes (ETGs), and neutral ionization.

#### 3.1. Electron temperature gradient modes

Electron temperature gradient modes are electrostatic instabilities which induce radial electron heat losses and hence are a possible candidate for the enhanced transport. A critical gradient

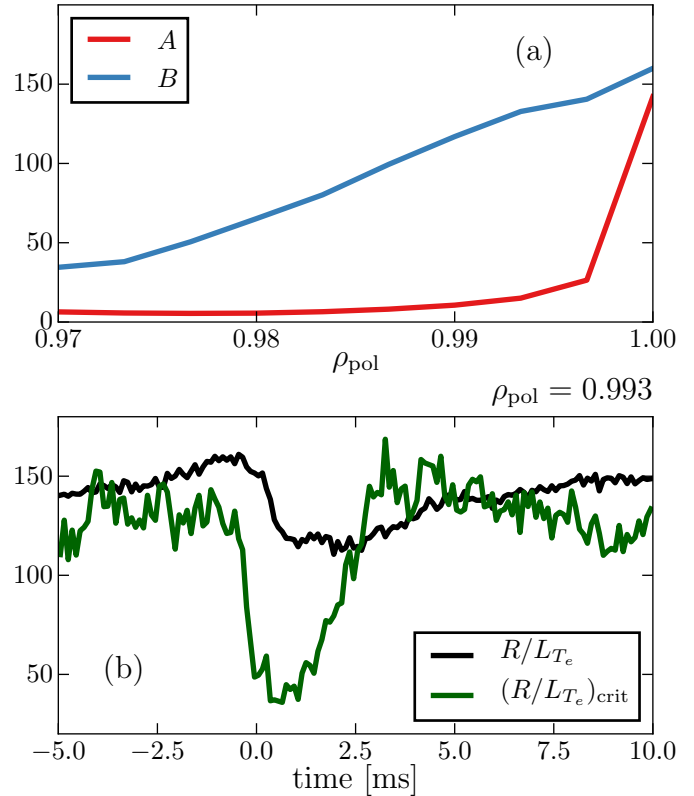


Figure 4: (a): Pre-ELM ( $-4 \text{ ms} < t < -2 \text{ ms}$ ) edge profile of the  $(R/L_{T_e})_{\text{crit}}$  terms in equation (2). (b): Evolution of  $R/L_{T_e}$  (black) and  $(R/L_{T_e})_{\text{crit}}$  (green) during an ELM cycle at  $\rho_{\text{pol}} = 0.993$ .

formula for the destabilization of the ETG has been derived from gyro-kinetic simulations in the core [29] and was extended to the edge [6]. If  $R/L_{T_e} > (R/L_{T_e})_{\text{crit}}$  then ETGs are destabilized, where  $(R/L_{T_e})_{\text{crit}}$  is

$$(R/L_{T_e})_{\text{crit}} = \max \begin{cases} A = (1 + \tau)(1.33 + 1.91\hat{s}/q) \cdot \\ (1 - 1.5\epsilon)[1 + 0.3\epsilon(d\kappa/d\epsilon)] \\ B = 1.2 \cdot R/L_{n_e} \end{cases} \quad (2)$$

and  $\tau = (1 + Z_{\text{eff}}T_e/T_i)$ ,  $\hat{s}$  is the magnetic shear,  $q$  is the safety factor,  $\epsilon$  is the inverse aspect ratio, and  $\kappa$  is the elongation of the magnetic surface. In figure 4a the profiles of  $A$  and  $B$  (see equation (2)) are shown. Given the strong  $\nabla n_e$  present at the edge, the term  $B$  is largely dominating the ETG stabilization as already pointed out in [6]. Hence, by comparing  $R/L_{T_e}$  (black) and  $(R/L_{T_e})_{\text{crit}} \approx 1.2 \cdot R/L_{n_e}$  (green) in figure 4b at  $\rho_{\text{pol}} = 0.993$ , i.e. in the steep gradient region, the existence of ETGs can be judged.

Right after the ELM-crash until roughly 2.5 ms,  $R/L_{T_e} > (R/L_{T_e})_{\text{crit}}$  suggesting that ETGs could be active in this phase. After that, due to the recovery of  $\nabla n_e$ ,  $R/L_{T_e} \approx (R/L_{T_e})_{\text{crit}}$  which indicates that the ETGs are suppressed. Note that the possible presence of ETGs in this phase is consistent with the reduced activity in the magnetics (see figure 2a). However, while the ETG activity is roughly consistent with the observation of additional transport delaying the recovery of  $\nabla T_e$ , ETGs should extend longer than  $\approx 2.5$  ms to reproduce the evolution in figure 2 in which  $\nabla T_e$  is fully recovered only 7 ms after the ELM-crash. On the other hand, equation (2) gives an indication of the relative strength of the ETGs since their onset is smooth [30, 31]. Hence, ETGs are probably still present when  $\nabla T_e$  is close to  $(R/L_{T_e})_{\text{crit}}$  but it is not clear yet how much of the total electron heat transport is actually induced by ETGs themselves. To access this point, dedicated gyrokinetic simulations including data from ions and electrons are foreseen.

### 3.2. Neutral ionization

Another possible mechanism which could delay the recovery of  $\nabla T_e$  is the energy lost in the ionization of the neutrals. Due to the strong density build up in the initial ELM-recovery phase, a large amount of neutrals needs to be ionized. To compare this loss channel to the other energy sinks and sources, transport simulations have been performed using the 1.5D transport code ASTRA [32, 33]. The results are presented in the following section.

Transport simulations generally solve a system of 1D diffusion equations, similar to the one derived in [34], for densities and temperatures of different plasma species. A variety of other modules are used to describe, for instance, auxiliary heating, MHD stability, current drive etc. Here, the neutral puff module of ASTRA is used to measure the loss of electron energy due to atomic processes during the ELM-recovery. By giving as input the measured density and temperature profiles together with the neutral influx  $\Gamma_N$ , radiative power and auxiliary heating power, it is possible to determine the sources and sinks of the ion  $P_i$

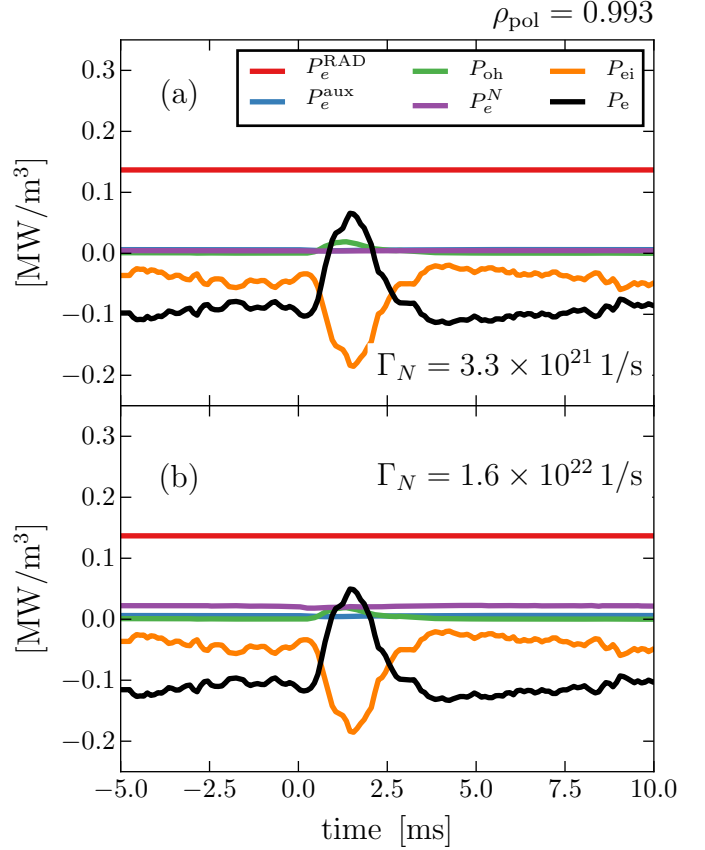


Figure 5: Modelled electron energy components during the ELM-recovery as defined in equations (3) at  $\rho_{\text{pol}} = 0.993$  for respectively  $\Gamma_N = 3.3 \times 10^{21}$  atoms/s (a) and  $\Gamma_N = 1.6 \times 10^{22}$  atoms/s (b).

and electron  $P_e$  energies. These are defined as follows:

$$P_e = P_{\text{oh}} + P_e^{\text{aux}} - P_{ei} - P_e^{\text{RAD}} - P_e^N \quad (3)$$

$$P_i = P_i^{\text{aux}} + P_{ei} - P_i^N \quad (4)$$

where  $P_{\text{oh}}$  is the ohmic power,  $P_e^{\text{aux}}$  and  $P_i^{\text{aux}}$  is the auxiliary ion and electron heating,  $P_{ei}$  is the electron-ion heat exchange,  $P_e^{\text{RAD}}$  is the power lost for radiation,  $P_e^N$  and  $P_i^N$  are the sum of the losses due to atomic processes (ionization, recombination, and charge exchange for the ions). By comparing  $P_e^N$  with the total  $P_e$ , the relative impact of atomic processes on the electron energy can be determined thus giving an idea if such losses could potentially affect the recovery of  $\nabla T_e$ . However, since the neutral fluxes are basically unknown within roughly two orders of magnitude ( $\Gamma_N \approx 10^{20} - 10^{22}$  atoms/s), a scan in  $\Gamma_N$  needs to be performed which, for simplicity, has been kept

constant during the ELM-recovery. Furthermore, the particle convection  $v$  at the plasma edge has been set to zero and only cold neutrals are considered at the energy of dissociated Franck-Condon neutrals of roughly 2.5 eV. A more consistent approach would be to perform predictive simulations of  $n_e$  by imposing different sets of particle diffusion coefficient  $D$ ,  $\Gamma_N$  and  $v$ , similarly to what was done in [35]. The interpretative simulations have been carried out on the discharge analyzed in [13] which had higher input power (5 MW) and consequently higher ELM-frequency ( $f \approx 80$  Hz) compared to the one shown in section 2.

Figure 5a and 5b show the single terms in equation (3) at  $\rho_{\text{pol}} = 0.993$  for respectively  $\Gamma_N = 3.3 \times 10^{21}$  atoms/s and  $1.6 \times 10^{22}$  atoms/s. In the case of  $\Gamma_N = 3.3 \times 10^{21}$  atoms/s (figure 5a)  $P_e^N$  (violet) is roughly a factor 50 smaller than  $P_e$  (black) and hence negligible. Since  $P_e^N \sim \Gamma_N$ , even by going to the extreme case of  $\Gamma_N = 1.6 \times 10^{22}$  atoms/s, the energy losses due to atomic processes remain too small to really affect the electron energy balance. Note that the ohmic (green) and the auxiliary (blue) heating contributions are also very small at these radial positions. On the other hand, the energy exchange between electrons and ions  $P_{ei}$  (orange) is the dominating term of  $P_e$  together with the radiation (red).  $P_e^{\text{RAD}}$  is kept constant during the entire ELM-cycle because an ELM-synchronized deconvolution of the bolometer measurements was too uncertain to be used.  $P_{ei}$ , instead, peaks right after the ELM-crash when, close to the separatrix,  $T_i \gg T_e$ . After that,  $T_i$  gets close to  $T_e$  and slightly rises until the next ELM crash [13] and so does  $P_{ei}$  since  $T_e$  stays roughly constant at the separatrix. Note that  $P_{ei}$  enters in the electron energy balance (equation (3)) with a negative sign and if  $T_i > T_e$ , as in this case,  $P_{ei}$  positively contributes to the total electron energy. The trend of  $P_{ei}$  after the ELM-crash is reminiscent of the recovery of  $\nabla T_e$  and might be one of the key parameters to understand the asymmetry between ion and electron temperature recovery. Note that, however, the local sinks and sources at the edge are much smaller than the energy flux arriving from the core plasma. Hence, the local dynam-

ics might be strongly influenced by the transport further inside the plasma.

#### 4. Summary and Outlook

Sub-ms measurements of the ion temperature and the impurity flows reveal a different time scale for the recovery of the maximum gradient of the ion and electron temperatures. The maximum of  $\nabla T_i$  and of  $\nabla n_e$  saturate roughly 3 ms after the ELM-crash together with the onset of mid frequency magnetic fluctuations ( $f < 50$  kHz) while  $\nabla T_e$  is recovered to the pre-ELM values only after 7.0 ms simultaneously with the establishment of high frequency fluctuations ( $f = 180$  kHz). Transport simulations show that the local energy sink due to atomic processes is negligible compared to the radiation loss and the ion-electron coupling. The trend of the latter resembles the recovery of  $\nabla T_e$  while ELM-resolved radiation profiles might be possible in the future. Finally, the destabilization of the electron temperature gradient modes is shown to quantitatively describe the enhanced electron energy transport required for delaying the recovery of  $\nabla T_e$ . However, a quantitative estimation of ETGs impact on the total heat transport requires dedicated gyro-kinetic simulations.

#### Acknowledgments

The authors gratefully acknowledge C. Angioni and D. Told for their help and advice regarding the electron temperature gradient mode physics. This work has been carried out within the framework of the EUROfusion Consortium and has received funding from the Euratom research and training programme 2014-2018 under grant agreement No 633053. The views and opinions expressed herein do not necessarily reflect those of the European Commission.

#### References

- [1] E. J. Doyle, et al., Nucl. Fusion 47 (2007) S18.
- [2] H. Zohm, Plasma Phys. Contr. Fusion 38 (1996) 105.
- [3] P. B. Snyder, et al., Phys. of Plasmas 9 (2002) 2037–2043.

- [4] D. Dickinson, et al., Plasma Phys. and Contr. Fusion 53 (2011) 115010.
- [5] S. Saarelma, et al., Nucl. Fusion 53 (2013) 123012.
- [6] D. Told, et al., Phys. of Plasmas 15 (2008) 102306.
- [7] P. Snyder, et al., Nucl. Fusion 51 (2011) 103016.
- [8] D. Hatch, et al., Nucl. Fusion 55 (2015) 063028.
- [9] A. Diallo, et al., Phys. Rev. Lett. 112 (2014) 115001.
- [10] F. M. Laggner, et al., Plasma Phys. and Contr. Fusion 58 (2016) 065005.
- [11] A. Diallo, et al., Phys. of Plasmas 22 (2015) 056111.
- [12] F. Mink, et al., Plasma Phys. and Contr. Fusion 58 (2016) 125013.
- [13] M. Cavedon, et al., Plasma Phys. and Contr. Fusion 59 (2017) 105007.
- [14] A. Burckhart, et al., Plasma Phys. and Contr. Fusion 52 (2010) 105010.
- [15] R. Behn, et al., Plasma Phys. and Contr. Fusion 49 (2007) 1289.
- [16] R. J. Groebner, et al., Nucl. Fusion 49 (2009) 045013.
- [17] M. N. A. Beurskens, et al., Nucl. Fusion 49 (2009) 125006.
- [18] K. H. Burrell, et al., Rev. of Sci. Instrum. 75 (2004) 3455–3457.
- [19] M. Cavedon, et al., Rev. of Sci. Instrum. 88 (2017) 043103.
- [20] H. Biglari, et al., Phys. of Fluids B: Plasma Phys. 2 (1990) 1.
- [21] P. B. Snyder, et al., Plasma Phys. and Contr. Fusion 46 (2004) A131.
- [22] M. R. Wade, et al., Phys. Plasmas 12 (2005) 056120.
- [23] D. Carralero, et al., Nucl. Fusion 57 (2017) 056044.
- [24] W. Kerner, et al., Nucl. Fusion 37 (1997) 493.
- [25] E. Viezzer, et al., Nucl. Fusion 55 (2015) 123002.
- [26] P. A. Schneider, et al., Plasma Phys. and Contr. Fusion 57 (2015) 014029.
- [27] L. Frassinetti, et al., Nucl. Fusion 57 (2017) 022004.
- [28] F. M. Laggner, et al., Phys. of Plasmas 24 (2017) 056105.
- [29] F. Jenko, et al., Phys. of Plasmas 8 (2001) 4096–4104.
- [30] W. Horton, Rev. Mod. Phys. 71 (1999) 735–778.
- [31] F. Jenko, et al., Physics of Plasmas 16 (2009) 055901.
- [32] G. V. Pereverzev, et al., ASTRA - Automated System for TRansport Analysis, Technical Report, IPP Report, 2002.
- [33] E. Fable, et al., Plasma Phys. and Contr. Fusion 55 (2013) 124028.
- [34] F. L. Hinton, R. D. Hazeltine, Rev. Mod. Phys. 48 (1976) 239–308.
- [35] M. Willensdorfer, et al., Nucl. Fusion 53 (2013) 093020.